

Collective modes in quasi-one-dimensional charge-density wave systems probed by femtosecond time-resolved optical studies

H. Schaefer,¹ V. V. Kabanov,^{2,3} and J. Demsar^{1,2,4}

¹Physics Department, Universität Konstanz, D-78457, Germany

²Zukunftskolleg, Universität Konstanz, D-78457, Germany

³Complex Matter Department, Jozef Stefan Institute, SI-1000, Ljubljana, Slovenia

⁴Institute of Physics, Ilmenau University of Technology, D-98693 Ilmenau, Germany

(Received 24 September 2013; revised manuscript received 17 December 2013; published 6 January 2014)

The interplay between the electronic and structural subsystems has strong implications on the character of collective excitations in cooperative systems. Their detailed understanding can provide important information on the coupling mechanisms and coupling strengths in such systems. With the recent developments in femtosecond time-resolved optical probes, numerous advantages with respect to conventional time-integrated probes have been put forward. Owing to their high dynamic range, high-frequency resolution, fast data acquisition, and an inherent access to phases of coherent excitations, they provide direct access to the interplay between various degrees of freedom. In this paper, we present a detailed analysis of time-resolved optical data on blue bronzes ($\text{K}_{0.3}\text{MoO}_3$ and $\text{Rb}_{0.3}\text{MoO}_3$), prototype quasi-one-dimensional charge-density wave (CDW) systems. Numerous coherent (Raman active) modes appear upon the phase transition into the CDW state. We analyze the temperature dependence of mode frequencies, their damping times, as well as their oscillator strengths and phases using the time-dependent Ginzburg-Landau model. We demonstrate that these low-temperature modes are a result of *linear* coupling between the Fermi surface nesting driven modulation of the conduction electron density and the normal-state phonons at the CDW wave vector, and determine their coupling strengths. Moreover, we are able to identify the nature of excitation of these coupled modes, as well as the nature of the probing mechanisms in this type of experiments. We demonstrate that in incommensurate CDW systems, femtosecond optical excitation initially suppresses the electronic density modulation, while the reflectivity changes at frequencies far above the CDW induced gap in the single-particle excitation spectrum are governed by the modulation of interband transitions caused by lattice motion. This approach can be readily extended to more complex systems with spatially modulated ground states.

DOI: [10.1103/PhysRevB.89.045106](https://doi.org/10.1103/PhysRevB.89.045106)

PACS number(s): 78.47.jg, 71.45.Lr, 72.15.Nj

I. INTRODUCTION

Understanding the interaction between different degrees of freedom seems to be crucial for the description of many novel advanced solid-state systems such as manganites, high- T_c superconductors [1], multiferroics, and/or (their) proximity coupled multilayers [2]. For studying the interplay between different subsystems, real-time femtosecond techniques are becoming increasingly important. Here, a femtosecond optical pulse is used to drive the system out of equilibrium, while the variably delayed light (from THz [3–6], visible [7] up to x-ray range [8]) or electron pulse [9,10] is utilized to track the relaxation back to equilibrium. One of the main advantages of these techniques is the ability to disentangle different spectrally overlapping components (excitations) based on their different temporal characteristics [5,6,11]. Moreover, resonant pumping schemes are recently being pursued giving access to dynamics following perturbation of a specific excitation [12–15]. In this way, the interplay between different excitations can be determined, clarifying their role in the functional properties of the material under scrutiny.

Low-dimensional charge-density wave (CDW) systems [16,17], where the low-temperature symmetry-broken state involves spatial modulation of both the conduction electron density and the underlying lattice, present a prototype system for investigating the interplay between the electronic and lattice degrees of freedom. In the past decade or so, various one- and two-dimensional CDWs have been studied by

time-resolved optical [18–25], photoemission [26–30], as well as structural probes [8–10]. The initial focus of research was in identifying various components in the observed photoinduced transients with the corresponding ones obtained by standard time-averaging spectroscopic techniques, as well as in coherent control of the collective modes [31]. It was shown that photoexcitation with an intense optical pulse can nonthermally quench the charge-density modulation which represents the electronic part of the charge-density wave [23,27]. Systematic studies of relaxation phenomena as a function of temperature and excitation density implied that the suppression of the carrier density modulation amplitude can be achieved on a time scale much faster than the time it takes for the lattice modulation to relax [9,23,30]. These observations imply that on a time scale comparable to the period of the characteristic lattice vibrations, the electronic and lattice components of the order parameter may follow different temporal trajectories.

Recent studies have demonstrated that Raman-active collective modes can be studied with unprecedented dynamic range and frequency resolution by all-optical pump-probe methods [24,25,32]. By studying reflectivity dynamics in the prototype quasi-one-dimensional CDW material $\text{K}_{0.3}\text{MoO}_3$ (commonly referred to as *blue bronze*), it was shown that numerous Raman-active modes appear upon lowering the temperature through the CDW transition temperature [24]. Low-temperature frequencies of these modes could be linked to frequencies of the phonons at the CDW modulation wave vector (\mathbf{q}_{CDW}) in the normal state, as measured by inelastic

neutron spectroscopy [33]. Importantly, most of these low-energy modes showed comparable (and incomplete) softening upon approaching the phase transition from below [24]. In order to determine the nature of these collective modes, the time-dependent Ginzburg-Landau (TDGL) analysis was applied. It was argued that most (but not all) of these low-temperature modes are a result of linear coupling of the phonon modes at \mathbf{q}_{CDW} with the modulated density of the conduction electrons. The incomplete softening of these modes, which seems to be a general feature in the class of quasi-one-dimensional CDW materials [18,20,22,32], was attributed to the fact that the spatially modulated conduction electron density does not adiabatically follow the ionic motion [24]. Finally, the subpicosecond overdamped component, whose decay time diverges near T_c and is commonly observed in many CDW compounds [18,20,22], was attributed to an overdamped amplitude mode of predominantly electronic character [24].

The results of the TDGL analysis applied to the experimental data on $\text{K}_{0.3}\text{MoO}_3$ (Ref. [24]) are summarized in Fig. 1. Here, the temperature evolution of the mode's frequencies and damping times is shown to be well reproduced by TDGL simulations. However, as opposed to the conventional equilibrium Raman spectroscopy, time-domain methods provide also access to phases of individual modes. The mode's amplitudes depend critically on the nature of excitation as well as probing

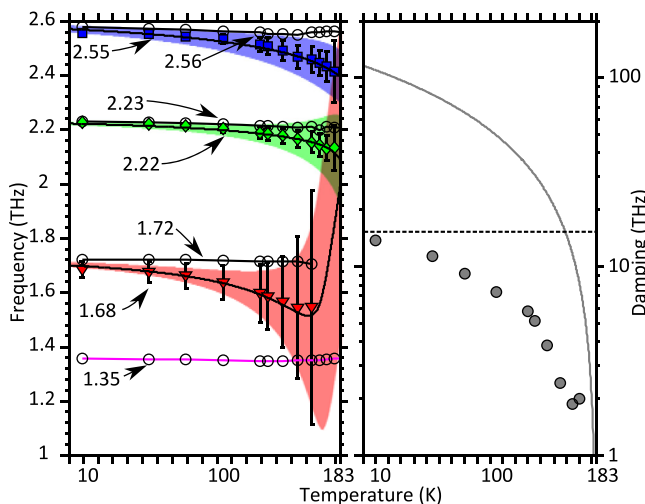


FIG. 1. (Color online) Comparison of experimental results on the prototype quasi-one-dimensional CDW $\text{K}_{0.3}\text{MoO}_3$ with the TDGL simulation. Left panel presents the temperature dependence of frequencies (solid symbols) and dampings (denoted by bars) of the three most intense oscillatory modes, all showing softening upon approaching $T_c = 183$ K. The low-temperature values of mode frequencies (in THz) are written. The TDGL model solution for eigenfrequencies (solid lines) and dampings (shaded areas whose widths correspond to damping) demonstrate an excellent agreement with the data (considering the simplicity of the model). Open symbols present frequencies of several weaker narrow modes, which were not included in the analysis. The right panel presents the temperature dependence of damping (solid symbols) of the fast overdamped component, demonstrating critical slowing down as T_c is approached. The solid line presents the TDGL prediction (a detailed discussion can be found in Sec. VI and in the Appendix), while the dashed line corresponds to the time resolution in this experimental configuration.

mechanism. Given the fact that the TDGL model nearly perfectly captures the evolution of the mode's frequencies and damping times, the analysis of the mode's amplitudes and phases within this model can provide important information on the nature of excitation of collective modes as well as the underlying probing mechanisms. These points were not elaborately addressed thus far.

The goal of this paper, which is essentially a followup of Ref. [24], is to address the above-mentioned aspects by reanalyzing the data on $\text{K}_{0.3}\text{MoO}_3$, focusing on temperature dependencies of the collective mode's phases and oscillator strengths. Here, the experimentally achieved high-frequency resolution and high dynamic range enable detailed comparison with TDGL predictions. We start by introducing the TDGL description of the dynamics of CDW systems (Sec. II). We show that different degrees of freedom, while being (linearly) coupled, exhibit different dynamics. By comparing experimental data to model predictions, we can thus shed light on the nature of the probing mechanism in the all-optical configuration (see Sec. III). Similarly, the phases of coupled modes and their temperature dependence provide important information as to the nature of excitation process (Sec. IV). In the earlier publication, several weak "satellite" modes in $\text{K}_{0.3}\text{MoO}_3$ showed qualitatively different temperature dependence as the most intense main modes [24]. It was argued that these modes might result from higher-order coupling. To resolve this question, we have performed additional measurements on $\text{Rb}_{0.3}\text{MoO}_3$, where the mode's splitting is much stronger than in $\text{K}_{0.3}\text{MoO}_3$. In Sec. V, we demonstrate that a closer look at the temperature dependence of oscillator strengths can be used to determine the order of coupling of the electron density modulation to the phonons. In particular, we show that in the blue bronzes ($\text{K}_{0.3}\text{MoO}_3$ and $\text{Rb}_{0.3}\text{MoO}_3$), all the observed symmetric, Raman-active (non-Goldstone [34]) modes of the low-temperature CDW phase are a result of linear coupling between the Fermi surface nesting driven conduction electron density modulation and normal-state phonons at the CDW wave vector. Finally, in Sec. VI, we address the overdamped components for completeness.

We should note that the presented analysis could be applied to model time-resolved optical data in a broader class of materials undergoing phase transitions into modulated ground states.

II. CHARGE-DENSITY WAVE ORDER-PARAMETER DYNAMICS WITHIN THE TIME-DEPENDENT GINZBURG-LANDAU FRAMEWORK

This section motivates and introduces the mathematical framework for the time-dependent Ginzburg-Landau analysis to analyze the dynamics of the coupled electron-lattice CDW system. Some graphical examples of selected solutions of the equation of motion are presented. We elaborate on derivations that were presented in an earlier publication [24], especially with respect to the case where multiple phonon modes are coupled to the electronic order.

Below the critical temperature (in blue bronze $T_c = 183$ K), new low-energy modes appear in the excitation spectrum. These are Raman-active modes, as recorded by Raman [35,36] or time-resolved optical spectroscopy [24], and

infrared active modes [37–39]. In order to describe the phase transition and the appearance of these modes, it is convenient to use the phenomenological theory of the second-order phase transitions with further application of equations of motion of Landau-Khalatnikov type. This approach allows one to describe qualitatively and in some cases even quantitatively the temperature dependence of the frequencies and dampings of modes induced by the phase transition.

Charge-density wave transition in solids is commonly related to the singularity in the electronic susceptibility at the certain wave vector, which makes the system unstable with respect to the periodic deformation corresponding to this wave vector (\mathbf{q}_{CDW}) [16]. This vector is usually incommensurate and does not coincide with a high-symmetry point of the Brillouin zone. In the simplest case, as in the case of *blue bronze* (space group C_{2h}^3), the phase transition is characterized by a propagation vector k_3 of the Brillouin zone according to Kovalev's notation [40]. This vector belongs to the two-prong star and corresponds to a non-Lifshitz point of the Brillouin zone. The two prongs of the star transform one to another via inversion. The phase transition is thus characterized by two nonidentical points (\mathbf{q}_{CDW} and $-\mathbf{q}_{\text{CDW}}$), whereby in blue bronze $\mathbf{q}_{\text{CDW}} = (1, 0.748, -0.5)$ [41].

As it is widely accepted, the application of Landau theory does not require the knowledge of the symmetry in the low-temperature symmetry-broken phase, i.e., this theory is based on the symmetry of the high-temperature phase only. Thus, the properties of the low-temperature incommensurate phase are determined by minimizing the thermodynamic potential and applying dynamic Landau-Khalatnikov equations. In general, there are two different approaches for describing the phase transition into an incommensurate CDW phase [42]. Within the first approach, the incommensurate phase is described as an intermediate phase between the high-temperature metallic (unmodulated) and the low-temperature commensurate CDW phase. Here, the incommensurate phase appears due to the presence of Lifshitz invariants (the terms in the free-energy expansion which are linear with the gradient of the order parameter), which lead to a discommensuration of the commensurate order parameter. The second approach is based on the construction of the order parameter that corresponds to the (experimentally determined) incommensurate wave vector. In this case, the Lifshitz invariants should be neglected since the phase transition occurs at this particular wave vector. In our case, it is more convenient to follow the latter approach.

For the above-mentioned incommensurate CDW state characterized by two nonidentical points (\mathbf{q}_{CDW} and $-\mathbf{q}_{\text{CDW}}$), the order parameter has two components which are proportional to $\exp(\pm i\mathbf{q}_{\text{CDW}}\mathbf{r})$. This means that the order parameter may be represented by a complex number $\tilde{\Delta}$, whereby $\tilde{\Delta}(-\mathbf{q}_{\text{CDW}}) = \tilde{\Delta}^*(\mathbf{q}_{\text{CDW}})$. The free-energy expansion has the form [42,43]

$$\phi = \phi_0 + \frac{\alpha}{2}(T - T_c)|\tilde{\Delta}|^2 + \frac{\beta}{4}|\tilde{\Delta}|^4, \quad (1)$$

where α and β are the Ginzburg-Landau constants and ϕ_0 the free-energy density of the high-temperature unmodulated phase. While there are no additional invariants in the incommensurate case, the situation is different in the commensurate case. Here, invariants of higher order in the order parameter, which explicitly depend on the phase of

the order parameter, are allowed. Since CDW modulation in $\text{K}_{0.3}\text{MoO}_3$ is incommensurate [33], we will not discuss the higher-order invariants further.

Below the critical temperature T_c , a nontrivial (nonzero) value of the order parameter appears:

$$|\tilde{\Delta}|^2 = \alpha(T_c - T)/\beta, \quad (2)$$

which is associated with the appearance of the conduction electron density modulation at the Fermi nesting wave vector.

In the low-temperature CDW phase, numerous oscillatory modes appear at $q = 0$, displaying pronounced softening when $T \rightarrow T_c$ from below. These modes are clearly no simple zone-folded phonons (in a strictly incommensurate state all phonons are folded to $q = 0$). However, these $q = 0$ modes can be a result of linear (or higher-order) coupling between the modulated conduction electron density at \mathbf{q}_{CDW} with normal-state phonons of the same symmetry at \mathbf{q}_{CDW} .

To describe this situation, we define $\mathbf{\Delta} = (\Delta_r, \Delta_i)$ as the (complex) order parameter associated with the electronic density modulation at the wave vector \mathbf{q}_{CDW} and refer to it as the *electronic part of the order parameter* (EOP). Conversely, the normal-state phonons at \mathbf{q}_{CDW} are referred to as *normal modes*. Thus, we include in the thermodynamic potential [see Eq. (3)] their normal coordinates which are coupled linearly to the order parameter [44]. In principle, such procedure is unnecessary if we consider thermodynamical properties only (when normal modes are left aside). However, as pointed out in Ref. [45], dynamic properties in this case (normal phonon modes linearly coupled to EOP) are significantly different. For illustrative purposes, we include only one lattice mode coupled to EOP and define the generalization of the expansion to multiple modes later (particularly when comparing the model predictions to the results on *blue bronze*). The free-energy expansion for this case is given by

$$\begin{aligned} \phi = \phi_0 + \frac{1}{2}\alpha(T - T_{c0})(\Delta_r^2 + \Delta_i^2) + \frac{1}{4}\beta(\Delta_r^2 + \Delta_i^2)^2 \\ + \frac{\Omega_0^2}{2}(\xi_r^2 + \xi_i^2) - m(\Delta_r\xi_r + \Delta_i\xi_i). \end{aligned} \quad (3)$$

Here, $\xi = (\xi_r, \xi_i)$ is the normal coordinate of the normal mode, which (generally) does not belong to the soft mode [24] and transforms as $\mathbf{\Delta}$. Ω_0 is the frequency of the normal mode at $T \gg T_{c0}$, m describes the coupling strength between the EOP and the normal mode, and $\alpha, \beta > 0$ are the Ginzburg-Landau constants. Here, T_{c0} is the bare critical temperature for the case of negligibly small coupling (when $m \rightarrow 0$). We assume that the effective mass of the mode is equal to 1.

Since the thermodynamic potential is phase independent in the case of incommensurate CDW order, we can choose $\xi_i^{(0)} = \Delta_i^{(0)} = 0$. Minimizing Eq. (3) with respect to Δ_r and ξ_r , we obtain the equilibrium solution

$$|\Delta_r^{(0)}| = \sqrt{\frac{m^2}{\beta\Omega_0^2} - \frac{\alpha}{\beta}(T - T_{c0})} = \sqrt{\frac{\alpha}{\beta}(T_c - T)}, \quad (4)$$

$$\xi_r^{(0)} = \frac{m\Delta_0}{\Omega_0^2}. \quad (5)$$

Here, $T_c = T_{c0} + \frac{m^2}{\alpha\Omega_0^2}$ is the experimentally observable T_c . We see that from the thermodynamics point of view, Eq. (3) is identical to Eq. (1). The linear coupling of the EOP (Δ) to normal coordinates ξ results in renormalization of the critical temperature only. We should point out that deformations belonging to $2\mathbf{q}_{\text{CDW}}$, $3\mathbf{q}_{\text{CDW}}$, $4\mathbf{q}_{\text{CDW}}$, \dots may only be coupled to higher orders of Δ (e.g., Δ^2 couples to normal modes at $2\mathbf{q}_{\text{CDW}}$) and will therefore not be taken into account.

Let us now focus on the dynamics of the coupled order parameter. Here, we are interested in small variations around equilibrium, where we define $x_{1,2}(t) = \Delta_{r,i}(t) - \Delta_{r,i}^{(0)}$ and $y_{1,2}(t) = \xi_{r,i}(t) - \xi_{r,i}^{(0)}$ (following the above definition $\Delta_i^{(0)} = \xi_i^{(0)} = 0$). We assume that in the soft-mode channel (the overdamped mode showing critical slowing down as T_c is approached from below [24,32]), the motion is strictly dissipative while the motion in the normal-mode channel is oscillatory. The assumption that the (predominantly) electronic mode is overdamped is based on the fact that its bare frequency $\hbar\omega = \sqrt{2}|\Delta|$ lies above the gap for single-particle excitations [16].

With this, the equations of motion describing Raman-active modes (for consistency we refer to the collection of symmetric modes as the *non-Goldstone channel* [34] from here on) have the following form:

$$\begin{aligned} \dot{x}_1 &= -2\kappa\alpha(T_c + \frac{m^2}{2\alpha\Omega_0^2} - T)x_1 - \kappa my_1, \\ \ddot{y}_1 &= -\Omega_0^2 y_1 - mx_1. \end{aligned} \quad (6)$$

Here, κ is the damping of the electronic mode in the absence of coupling. Importantly, Eqs. (6) are *decoupled* from the equations of motion in the *Goldstone channel* that describe the infrared active modes

$$\dot{x}_2 = -\kappa \frac{m^2}{\Omega_0^2} x_2 - \kappa my_2, \quad \ddot{y}_2 = -\Omega_0^2 y_2 - mx_2. \quad (7)$$

Equations (6) and (7) describe the overdamped and oscillatory excitations in the non-Goldstone and Goldstone channels, respectively, including the amplitude and the phase modes. Here, each coupled phonon mode at $\pm\mathbf{q}_{\text{CDW}}$ generates in the low-temperature phase one Raman-active and one infrared-active mode [34,39,46] with eigenfrequencies close to the frequency of the corresponding normal modes.

First, we demonstrate that the standard amplitude and phase mode relations can be recovered from these equations. If we assume that the adiabatic condition is fulfilled ($\kappa \rightarrow \infty$), which means that the dynamics in the EOP is fast and adiabatically follows the ionic motion, we obtain the temperature dependence of the amplitude mode [16]; i.e., $\Omega \rightarrow 0$ as $T \rightarrow T_c$:

$$\Omega = \Omega_0 \sqrt{\frac{T_c - T}{T_c + \frac{m^2}{2\alpha\Omega_0^2} - T}}.$$

Similarly, in the adiabatic limit, Eqs. (7) lead to the known result that the phase mode is gapless, i.e., it has zero frequency at $q = 0$ and is a true Goldstone mode.

The general solution of Eqs. (6) can be found by the ansatz $x_1 = a_1 \exp(\lambda_1 t)$ and $y_1 = b_1 \exp(\lambda_1 t)$ resulting in a cubic equation for λ_1 :

$$\begin{aligned} \lambda_1^3 + 2\kappa\alpha \left(T_c - T + \frac{m^2}{2\alpha\Omega_0^2} \right) \lambda_1^2 + \Omega_0^2 \lambda_1 \\ + 2\kappa\alpha\Omega_0^2(T_c - T) = 0. \end{aligned} \quad (8)$$

One of the roots $\lambda_1^{(1)}$ is real and negative below T_c reaching $\lambda_1^{(1)} = 0$ at $T = T_c$. This root corresponds to an overdamped mode, whose relaxation time diverges near T_c and thus represents the true soft mode of the system. The other two roots are complex conjugate [at $T = T_c$ the roots are given by $\lambda_1^{(2,3)} = \pm i\Omega_0 \sqrt{1 - (\frac{\kappa m^2}{2\Omega_0^3})^2 - \frac{\kappa m^2}{2\Omega_0^2}}$]. Here, the real part $\Gamma = \text{Re}\lambda_1$ is the damping, while the imaginary part $\Omega = \text{Im}\lambda_1$ is the frequency of the non-Goldstone excitation.

Similar derivation shows that in the Goldstone mode sector, describing infrared-active modes given by Eqs. (7), one root is given by $\lambda_2^{(1)} = 0$. This indicates that the thermodynamic potential does not depend on the phase of the order parameter (as already previously stipulated), and the phase mode is (naturally in the absence of pinning) a true Goldstone mode with zero frequency at $q = 0$. The two other roots are also temperature independent, $\lambda_2^{(2,3)} = \pm i\Omega_0 \sqrt{1 - (\frac{\kappa m^2}{2\Omega_0^3})^2 - \frac{\kappa m^2}{2\Omega_0^2}}$. Here, $\Gamma = \text{Re}\lambda_2$ is the damping while $\Omega = \text{Im}\lambda_2$ is the frequency of the new infrared-active mode at the zone center which appears below T_c . Note that at T_c the frequencies of the mode(s) in the non-Goldstone sector are exactly equal to the frequencies of the corresponding modes in the Goldstone sector.

The solution of Eqs. (6) thus yields the eigenmodes as a function of temperature. Figure 2 shows the temperature dependence of the frequency and damping of the oscillatory mode, as well as the damping of the overdamped mode. The two examples correspond to the adiabatic coupling regime

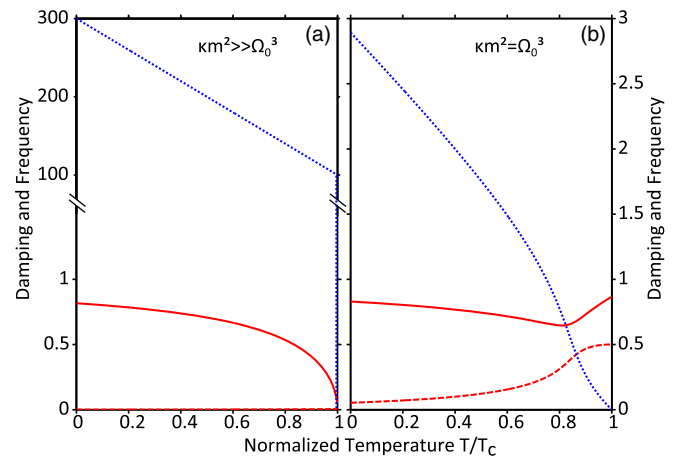


FIG. 2. (Color online) The temperature evolution of the eigenvalues of the collective excitations (mode frequencies and dampings) as predicted by the TDGL. The dotted (blue) line represents the damping of the overdamped mode, while the solid and dashed (red) lines represent, respectively, the frequency and damping of the oscillatory mode. Panel (a) presents the adiabatic coupling limit ($\kappa m^2 \gg \Omega_0^3$), while panel (b) shows the results for the nonadiabatic case, where $\kappa m^2 = \Omega_0^3$.

[Fig. 2(a)] where $\kappa m^2 \gg \Omega_0^3$, and the nonadiabatic regime [Fig. 2(b)], where $\kappa m^2 \approx \Omega_0^3$. While the adiabatic case leads to a true soft-mode behavior, with frequency of the oscillatory mode going to zero near T_c , this is not true in the nonadiabatic case. In the latter case, we observe only partial softening of the oscillatory mode while damping of the true soft mode shows critical behavior near T_c .

Because the infrared modes are silent in the optical pump-probe configuration in systems with inversion symmetry and since the thermodynamic potential does not depend on the phase we adopt $\text{Im}\Delta, \text{Im}\xi = 0$ and omit (r, i) indices for simplicity. Generalization of the thermodynamic potential to the case of multiple modes interacting with EOP is straightforward. In the general case of n -normal modes with frequencies Ω_l ($1 < l < n$) linearly coupled to Δ , we have to substitute $\Omega_0^2 \xi^2/2 \rightarrow \Omega_l^2 \xi_l^2/2$ and $m\Delta\xi \rightarrow m_l \Delta\xi_l$ in Eq. (3) and sum over all normal modes. Accordingly, the equilibrium values of $\Delta_0, \xi_{0,l}$ (from here on $\Delta_r^{(0)} = \Delta_0$ and $\xi_{r,l}^{(0)} = \xi_{0,l}$, or simply ξ_0 in case of a single normal mode coupled to Δ) are given by

$$\Delta_0 = \sqrt{\frac{\alpha}{\beta}(T_c - T)} \quad \text{with} \quad T_c \equiv T_{c0} + \sum_{l=1}^n \frac{m_l^2}{\alpha \Omega_l^2}, \quad (9)$$

$$\xi_{0,l} = \frac{m_l \Delta_0}{\Omega_l^2}.$$

Here, l numerates the normal modes which are coupled linearly to Δ . The equations of motion for the case of coupling of n -normal modes are also very similar to Eq. (6):

$$\frac{1}{\kappa} \dot{x} = -\frac{\partial^2 \phi}{\partial \Delta^2} x - \sum_l \frac{\partial^2 \phi}{\partial \Delta \partial \xi_l} y_l, \quad (10)$$

$$\Gamma_l \dot{y}_l + \ddot{y}_l = -\frac{\partial^2 \phi}{\partial \Delta \partial \xi_l} x - \frac{\partial^2 \phi}{\partial \xi_l^2} y_l.$$

All partial derivatives are taken at the equilibrium values of Δ_0 and $\xi_{0,l}$. For generality, we introduced also internal dampings Γ_l of normal modes. These were neglected in Eqs. (6) and (7) since it was shown that the temperature dependence of damping is mainly governed by coupling to Δ (see Fig. 6 in Ref. [47]). Equations (10) describe the complete dynamics in the non-Goldstone sector and can be solved numerically, with the number of equations increasing with the number of normal modes involved.

It is interesting to look at the model solution if two or more normal modes are coupled to Δ . Figure 3 presents the result of simulations with two normal modes of similar frequency ($\Omega_2/\Omega_1 = 1.2$) coupled to Δ . Figure 3(a) presents the case where the coupling of both modes to Δ has the same strength, i.e., $m_2 = m_1 = m$. It is obvious that the lower-frequency mode shows much stronger renormalization as the higher-frequency mode. If the coupling strength for the high-frequency mode (Ω_2) is substantially higher than that of the mode with lower frequency, the situation can be reversed as shown in Fig. 3(b), where $m_2 = m$ and $m_1 = m/10$. Finally, if the coupling strengths are further increased ($m_2 = 2m$ and $m_1 = m/5$), an avoided crossing can be realized [Fig. 3(c)] very similar to recent observations in the rare-earth tellurides [22] [Fig. 3(d)].

From this analysis, it follows that in an incommensurably modulated ground state any normal mode being linearly

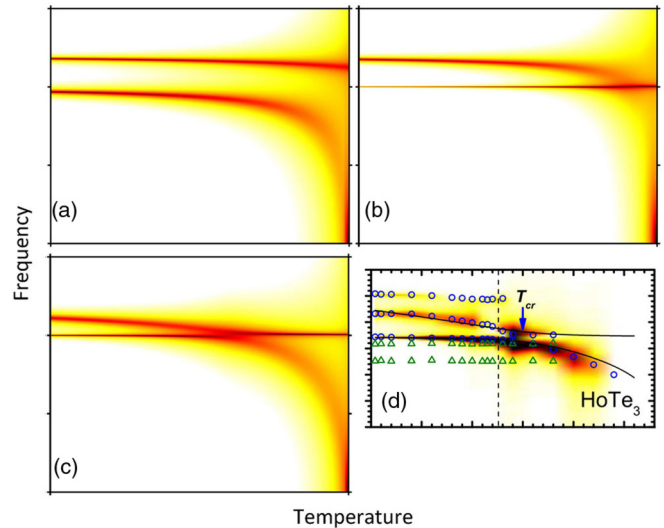


FIG. 3. (Color online) Temperature evolution of the eigenvalues of the collective excitations as predicted by the TDGL for two coupled normal modes with $\Omega_2 = 1.2\Omega_1$. (a) Identical coupling strength for both modes $m_2 = m_1$. (b) Stronger coupling of the high-frequency mode $m_2 = 10m_1$. (c) The same as in (b) yet both coupling constants increased by a factor of 2. The color coding represents the spectral weight and shape of the modes as probed via electronic response, neglecting any effects of excitation or probing mechanism (discussed in Secs. III and IV). (d) Experimental data on HoTe_3 , adapted from Ref. [22].

coupled to the underlying electronic instability results in a pair of modes in the low-temperature phase. One of them is an infrared-active mode in a Goldstone channel, while the other is Raman-active mode in the non-Goldstone channel. In the absence of intrinsic damping, only the modes in the non-Goldstone channel are found to exhibit temperature dependence. The extent of damping and softening depends strongly on coupling strengths, so that situations like avoided crossing can be realized. The true soft mode of the system is found to be an overdamped mode of predominantly electronic nature.

III. PROBING MECHANISM

When using optical time-resolved (pump-probe) experiments, where two light pulses are used to excite and probe the sample, the understanding of the light-matter interaction is important for proper data evaluation. This section discusses the probing mechanism while the next will discuss the details of photoexcitation.

Given the linear coupling between the normal mode and the electronic modulation, both of them contain contributions of the overdamped and oscillating responses. One question to be answered is which normal coordinate and the associated normal mode is actually reflected in the time traces of photoinduced reflectivity recorded in the all-optical pump-probe experiment.

In the pump-probe experiment the induced change in reflectivity δR is generally given by

$$\delta R = \frac{\partial R}{\partial \varepsilon_1} \delta \varepsilon_1 + \frac{\partial R}{\partial \varepsilon_2} \delta \varepsilon_2,$$

where ε_1 and ε_2 are the real and imaginary components of the dielectric function $\varepsilon(q = 0, \hbar\omega)$, which is in general a tensor. At optical frequencies ($\hbar\omega$ much larger than CDW induced gap in the single-particle excitation spectrum), we can expand the dielectric constant in the vicinity of the CDW phase transition in powers of order parameters Δ and ξ . Thus, $\varepsilon(q = 0, \hbar\omega)$ has the following form:

$$\varepsilon_j(\Delta, \xi) = \varepsilon_{j,0} + \frac{c_{j,0}}{2} \Delta^2 + \frac{c_{j,1}}{2} \xi^2 + c_{j,2} \Delta \xi. \quad (11)$$

Here, $\varepsilon_{j,0}$ ($j = 1, 2$) is the dielectric constant of the high-temperature phase, while $c_{j,0}$, $c_{j,1}$, and $c_{j,2}$ are constants. Linear terms in Δ or ξ are not allowed by symmetry and higher-order terms such as Δ^4 , $\Delta^2 \xi^2$ are neglected. Constants $\varepsilon_{j,0}$, $c_{j,0}$, $c_{j,1}$, etc., are in principle temperature dependent, but below T_c the temperature dependence of the order parameter normally dominates the variation of the dielectric function. Therefore, we assume $\varepsilon_{j,0}$, $c_{j,0}$, $c_{j,1}$, and $c_{j,2}$ to be temperature independent.

For small perturbations, the resulting changes in the dielectric function can be expanded to

$$\delta\varepsilon_j = c_{j,0} \Delta_0 \delta\Delta + c_{j,1} \xi_0 \delta\xi + c_{j,2} (\Delta_0 \delta\xi + \xi_0 \delta\Delta). \quad (12)$$

Thus, the photoinduced change in reflectivity below the phase transition is given by

$$\delta R(\propto |\delta\varepsilon|) = \Delta_0 (a_1 \delta\Delta + a_2 \delta\xi). \quad (13)$$

Here, we made use of the fact that $\xi_0 \propto \Delta_0$ [see Eq. (9)] and introduced new proportionality constants a_1 and a_2 .

Since EOP and normal modes are linearly coupled, all of them contain contributions of the overdamped and oscillating responses. To demonstrate that, it is instructive to plot the time evolution of $\delta\Delta(t) = \Delta(t) - \Delta_0$ and $\delta\xi_l(t) = \xi_l(t) - \xi_{0,l}$ following the perturbation of the system. Figure 4(a) presents the time evolution of $\delta\Delta(t)$ and $\delta\xi_1(t)$ following the instantaneous suppression of Δ at time zero. Here, we considered the case

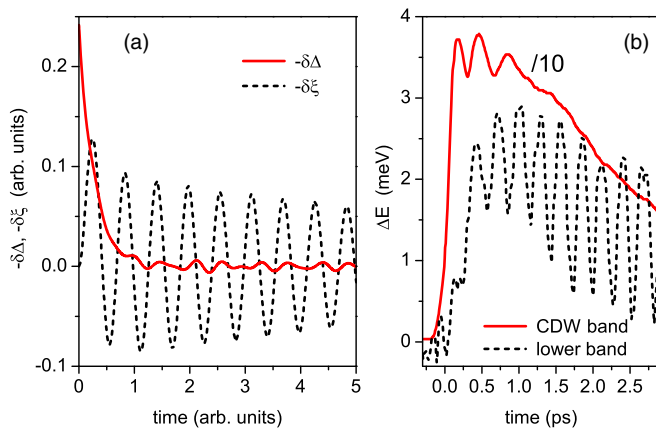


FIG. 4. (Color online) (a) The time evolution of $\delta\Delta(t)$ and $\delta\xi_1(t)$, for the case of three modes ($\Omega_3 = 1.15\Omega_2 = 1.5\Omega_1$) coupled to Δ with the same coupling constant m . For the initial condition ($t = 0$), we assumed a suppressed Δ while $\delta\xi_1(0) = 0$. (b) The temporal evolution of the shift of the binding energy for the CDW band (solid line) and lower band (dashed) in TbTe_3 ($T = 100$ K, excitation density is 2 mJ/cm 2) recorded by time-resolved photoemission (adapted from Ref. [28]).

of three normal modes ($\Omega_3 = 1.15\Omega_2 = 1.5\Omega_1$) coupled to Δ with the same coupling constant m . While the dominant contribution to $\delta\Delta(t)$ is the overdamped mode, all three oscillatory modes are also revealed. The same goes for $\delta\xi_1(t)$, whereby the dominant contribution is the one oscillating with frequency close to Ω_1 (coupling to Δ gives rise to damping which slightly modifies the frequency [48]).

Generally, it is expected that the ratio of the overdamped and oscillatory components depends on the probe photon energy [see Eq. (13)]. In the case of probe photon energy matching some band to band optical transition the oscillatory components may largely dominate the response.

To illustrate this point, we present here the recent data on CDW system TbTe_3 [Fig. 4(b)] obtained by time-resolved photoemission [28]. While the dynamics of the CDW band is largely dominated by a damped electronic response, the dynamics of the band at the binding energy of -0.5 eV (data recorded at high excitation densities are presented) shows a predominantly oscillatory response.

From the above discussion, it follows that spectrally resolved studies have to be performed in order to pinpoint the microscopic mechanism of the probe process, i.e., to determine what is the dominant term giving rise to reflectivity change at optical frequencies. However, as noted, due to the linear coupling between the EOP and normal modes, all of the collective modes should be observed, provided that the signal-to-noise level is high enough.

IV. PHOTOEXCITATION MECHANISM

It was demonstrated on several CDW systems that the data on the temperature dependence of frequencies and dampings of the collective modes, recorded by time-resolved optical methods, have superior dynamic range and frequency resolution [22–25, 32] to standard Raman spectroscopy. In addition, the time-domain approach provides us with the temperature dependence of phases and amplitudes of the oscillatory components. The two naturally depend on the nature of photoexcitation and probing mechanisms. In this and the following sections, the expected temperature dependencies of phases and amplitudes of the non-Goldstone modes will be discussed for different excitation scenarios and compared to the experimental data. To do so, we first derive solutions of Eqs. (10) by considering the interaction of the system with a short optical pulse.

The coupling of the laser field $\vec{E}(t)$ with normal coordinates is governed by the force tensor. According to Refs. [49] and [50], the force tensor is similar to a Raman tensor, where forces acting on normal coordinates Δ , ξ_i are given by [50]

$$F_v(t) = \sum_{i,j} \int_{-\infty}^t E_i(\tau) \chi_{i,j}^v(t - \tau) E_j^*(\tau) d\tau. \quad (14)$$

Here, i and j denote the symmetry directions of the force tensor $\chi_{i,j}$ and v numerates invariants appearing in the free-energy expansion. In the transparent media, force tensor coincides with the Raman tensor. In absorbing media, however, the imaginary part of the force tensor is essentially different from the Raman tensor. The integral over τ takes into account the retardation (memory) effects, which are usually caused

by the imaginary part of the force tensor [49,50]. In the case of retardation, $F_v(t)$ may substantially differ from the instantaneous response to the electric field. The resulting force $F_v(t)$ can act on any normal mode including the totally symmetric (A_g) and other Raman-active modes in the low-temperature phase.

Since susceptibilities are defined as negative derivatives of the thermodynamic potential, the forces may be approximated by

$$\begin{aligned} F_\Delta &= -G(t)(A\Delta_0 - \mu\xi_0), \\ F_\xi &= -G(t)(\gamma\xi_0 - \mu\Delta_0). \end{aligned} \quad (15)$$

Here, A , μ , and γ are constants proportional to the interaction strength of the external electric field with different normal modes [see Eq. (14)]. The time dependence of different susceptibilities [Eq. (14)] may in general be different. Here, for simplicity, we assume their temporal characteristics to be identical, and parametrize all interaction channels with a single time-dependent function $G(t)$. The sign in front of the cross/coupling terms ($\mu\xi_0$ and $\mu\Delta_0$) in Eqs. (15) is chosen to be negative to match the definition in Eq. (3).

We first consider the simplest case of one coupled normal mode, where $x(t) = \Delta(t) - \Delta_0$ and $y(t) = \xi(t) - \xi_0$. Substituting the generalized forces into the equations of motion [Eqs. (10)], we obtain

$$\begin{aligned} \frac{1}{\kappa}\dot{x} &= -\frac{\partial^2\phi}{\partial\Delta^2}x - \frac{\partial^2\phi}{\partial\Delta\partial\xi}y + F_\Delta, \\ \Gamma\dot{y} + \ddot{y} &= -\frac{\partial^2\phi}{\partial\Delta\partial\xi}x - \frac{\partial^2\phi}{\partial\xi^2}y + F_\xi. \end{aligned} \quad (16)$$

Here, all partial derivatives are calculated at the equilibrium values Δ_0 and ξ_0 . After evaluating all second derivatives of the thermodynamic potential and replacing \ddot{y} by a new variable \dot{z} (in order to keep only first-order time derivatives), the equations of motion can be represented by the following matrix equation:

$$\begin{aligned} -\begin{pmatrix} \dot{x} \\ \dot{y} \\ \dot{z} \end{pmatrix} &= \begin{pmatrix} M_{1,1} & -\kappa m & 0 \\ 0 & 0 & -1 \\ -m & \Omega_0^2 & \Gamma \end{pmatrix} \begin{pmatrix} x(t) \\ y(t) \\ z(t) \end{pmatrix} \\ &- \begin{pmatrix} F_\Delta(t) \\ 0 \\ F_\xi(t) \end{pmatrix}. \end{aligned} \quad (17)$$

Here, the matrix element $\underline{M}_{1,1}$ is $M_{1,1} = \kappa(\alpha + 3\beta\Delta_0^2)$.

Let us first solve the homogeneous part of Eq. (17). The transformation of the homogeneous part of the equation from the time to frequency space is realized via the ansatz

$$\begin{pmatrix} x(t) \\ y(t) \\ z(t) \end{pmatrix} = \tilde{\mathbf{x}}e^{\lambda t}, \quad (18)$$

leading to the eigenvalue problem $-\lambda\tilde{\mathbf{x}} = \underline{M}\tilde{\mathbf{x}}$. The solution is given by the diagonal eigenvalue matrix $\underline{\Lambda}$ (λ_i 's are the diagonal elements) and eigenvector matrix \underline{S} , giving the

general solution

$$\mathbf{x}(t) = \underline{S} \begin{pmatrix} E_1 e^{\lambda_1 t} \\ E_2 e^{\lambda_2 t} \\ E_3 e^{\lambda_3 t} \end{pmatrix}, \quad (19)$$

where E_i 's are complex parameters defined by the boundary conditions.

For the inhomogeneous part of Eq. (17), we first assume the temporal dependence of the driving force $G(t)$ to be a simple step function [$G(t) = 0$ for $t < 0$ and $G(t) = 1$ for $t \geq 0$]. This is physically motivated by the fact that photoexcitation in opaque medium results in absorption, i.e., generation of excess quasiparticles. In view of the theory of coherent phonon generation [50], this would correspond to the displacive excitation limit [48,50]. In the first approximation, we thus assume that the recovery of excess quasiparticle density is slow, leading to the above-mentioned steplike driving force (the effect of finite relaxation time is addressed in the Appendix).

Depending on the interaction strengths between the driving force and the normal modes (determined by parameters A , μ , and γ), we can formally distinguish between three excitation processes. Here, parameter A corresponds to a change in the electronic system (e.g., heating of electrons), μ corresponds to a change in the coupling strength between the electron density modulation and the phonon mode, and γ accounts for a change in the elastic constants of the lattice.

The solution of Eq. (17) for a steplike excitation can be further simplified by considering that in a harmonic system a steplike force is equivalent to a sudden change in the equilibrium position. Therefore, we choose the initial conditions for x and y at zero time delay ($t = 0$) to correspond to a shift of equilibrium positions of Δ and ξ [48]. In other words, upon excitation at $t = 0$ the equilibrium values Δ_0 and/or ξ_0 are instantaneously reduced (similarly to the displacive mechanism of coherent phonon generation) [48]. The initial conditions [we further assume that $\dot{\mathbf{x}}(t = 0) = 0$] define the phases as well as the amplitudes of the eigenmodes via Eqs. (18) and (17):

$$\underline{M}\mathbf{x}(t = 0) = -\begin{pmatrix} F_\Delta \\ 0 \\ F_\xi \end{pmatrix} = \underline{M}\underline{S} \begin{pmatrix} E_1 \\ E_2 \\ E_3 \end{pmatrix}. \quad (20)$$

We will now restrict the discussion to the two extreme scenarios where photoexcitation primarily results in a change of Δ_0 or ξ_0 (for both cases $\mu = 0$).

Case 1. $A > 0$ (while $\gamma = \mu = 0$). A is chosen to be positive in order for the perturbation to result in a suppression of the order upon excitation. The resulting forces are

$$F_\Delta(t = 0) = -A\Delta_0, \quad F_\xi(t = 0) = 0. \quad (21)$$

Moreover, for the case of a weak perturbation regime, $|A| \ll |\alpha(T - T_c)|$ has to be satisfied.

Case 2. $\gamma > 0$ (while $A = \mu = 0$). γ is again chosen to be positive in order for the perturbation to result in a suppression of the order upon excitation. The resulting forces are

$$F_\Delta(t = 0) = 0, \quad F_\xi(t = 0) = -\gamma\xi_0 = -\gamma\frac{m}{\Omega_0^2}\Delta_0. \quad (22)$$

Following the same reasoning as above, γ is presumed to be small, i.e., $|\gamma|m \ll \Omega_0^2$.

As discussed in Sec. III, the measured signal can be governed either by probing the electronic order (Δ), the lattice order (ξ), or both of them [see Eq. (13)]. Assuming that one of the probing mechanisms is dominant, we can distinguish four possible scenarios: (a) probing and excitation both occur via EOP, (b) we perturb the EOP (Δ) but probe the lattice order (ξ), (c) we perturb the lattice order and probe the EOP, or (d) probing and excitation both occur via the lattice order.

The above four scenarios can be confronted by comparing the model simulations for each of the scenarios with experimental data on $\text{K}_{0.3}\text{MoO}_3$. In all simulations, three normal modes linearly coupled to the EOP are considered. We used the mode-coupling strengths extracted by analyzing the temperature dependence of frequencies and dampings [24]: $\kappa m_1^2 = 600 \text{ THz}^3$ for the 1.68-THz mode, $\kappa m_2^2 = 325 \text{ THz}^3$ for the 2.22-THz mode, and $\kappa m_3^2 = 1200 \text{ THz}^3$ for the 2.55-THz mode. Moreover, for simplicity, we assumed that γ_i 's are the same for all normal coordinates. In the case when it is assumed that the dynamics is probed via the lattice orders we use prefactors ($\frac{m_i}{\Omega_i^2}$) to scale the response according to the factor that is found for the excitation interaction [see Eq. (22)]. Finally, to enable one to one comparison, the measured amplitudes were normalized such that the experimentally measured amplitude of the 1.68-THz mode matches its simulated value at low temperatures.

The model simulations for the above four scenarios (lines) are compared to the data (symbols) in Fig. 5. The scenarios 5(b) and 5(c) can well reproduce the nearly temperature-independent mode amplitudes (up to $\approx 150 \text{ K}$) as observed experimentally. In contrast, if probing and excitation occur via the same channel, the mode amplitudes either increase or decrease with temperature in this temperature range. From this, we conclude that excitation and probing do not occur via the same channel.

Scenario 5(c) describes excitation of the lattice by changing the bare phonon frequencies as defined by Eq. (22). In order for this type of excitation to result in a suppression of ξ_0 , it has to correspond to a hardening of the bare phonon mode(s). Typically, photoexcitation results in a phonon softening rather than hardening, thus this scenario seems unlikely, despite the fact that photoinduced phonon hardening has been observed on ultrashort time scales in special cases [51]. Far more plausible seems to be scenario 5(b), where photoexcitation initially perturbs the EOP, while the optical response is dominated by the lattice motion. This scenario is also consistent with high perturbation experiments where signatures of transient melting of the electronic order were found at excitation densities comparable to the electronic part of the condensation energy [22,23].

Apart from the temperature dependence of mode amplitudes, the above scenarios can be tested by comparing the measured temperature dependencies of phases of the oscillatory modes ϕ with results from model simulations. In Fig. 6, the temperature dependence of phases $\{\text{defined by } \cos[2\pi\nu(t - t_0) + \phi]\}$ of the three dominant oscillatory components [$\nu_1 = 1.68 \text{ THz}$ (circles), $\nu_2 = 2.22 \text{ THz}$ (squares), and $\nu_3 = 2.55 \text{ THz}$ (crosses)] in $\text{K}_{0.3}\text{MoO}_3$ are plotted and compared with the model simulations for scenarios 6(b) (left

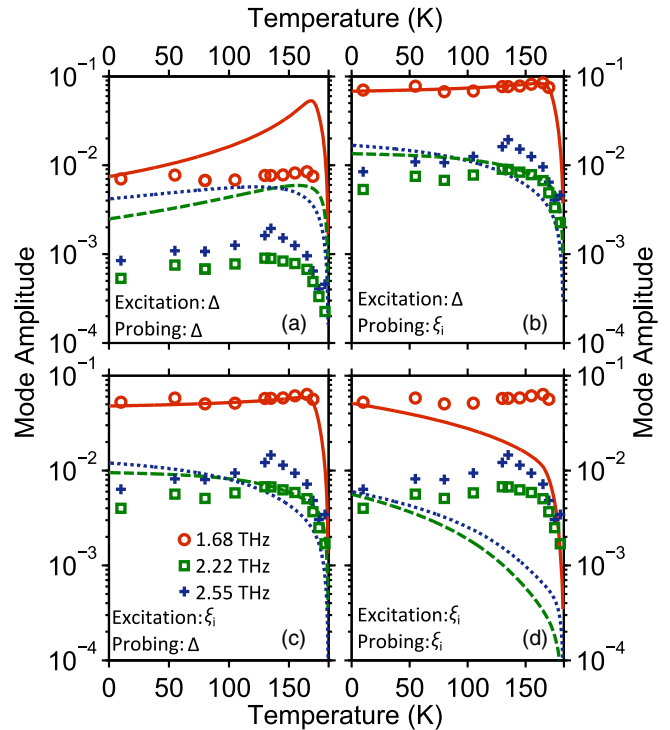


FIG. 5. (Color online) The temperature dependence of the amplitudes of the oscillatory modes compared to simulations based on different excitation/probing scenarios (see text). The lines represent model solutions while the symbols show the experimental data. The colors/symbol shapes/line styles for the three dominant modes are as follows: 1.68-THz mode, red/open circle/straight line; 2.22-THz mode, green/open square/dashed line; and 2.55-THz mode, blue/cross/dotted line. The simulated amplitudes were scaled such that the simulated amplitude for the 1.68-THz mode matches the experimental data in the zero-temperature limit.

panel) and 6(d) (right panel). Also, here the case where probing and excitation occurs through different channels (left panel) fits the experimental data better.

For simplicity, the driving force $G(t)$ was considered to be a simple step function. The model simulations can be extended to the case where the driving force is short lived. As shown in the Appendix, the effect of the finite lifetime of the driving force can be revealed in the temperature dependence of the rise-time dynamics. Again, the qualitative agreement between the experimental data and the TDGL simulations is surprisingly good.

To summarize, based on the experimental data on temperature dependence of the mode's amplitudes and phases, we conclude that photoexcitation initially perturbs the electronic order while the resulting changes in the dielectric constant reflect the dynamics of the lattice order parameter. This is supported by observations that the electronic order could be transiently quenched without collapsing the periodic lattice modulation [23].

V. ORIGIN OF WEAK SATELLITE MODES

In addition to the three dominant oscillatory modes discussed above, there are numerous additional modes observed in $\text{K}_{0.3}\text{MoO}_3$ [24,47]. Most of the modes appear only below

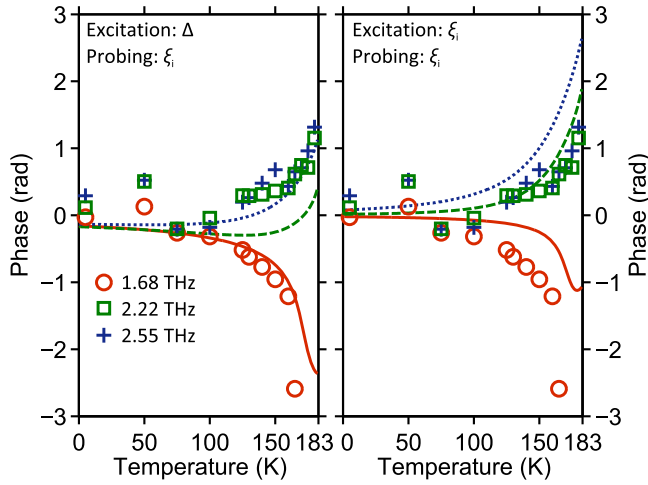


FIG. 6. (Color online) The temperature dependence of experimentally measured phases of the oscillatory modes (symbols) compared to the model simulations. Color/line style assignment is the same as in Fig. 5. The left panel shows the model solution for the case of primary excitation of the electronic order, while the right panel shows the simulation for the case of excitation through the lattice order. For both cases, probing occurs via the lattice order.

the phase transition temperature, but some are seen also in the metallic state (albeit with a dramatically reduced amplitude). The natural question to be answered is whether all these modes are linearly coupled to Δ or higher-order coupling terms need to be included (which we commonly neglected thus far).

One physical observable that might be able to distinguish between the linear and higher-order coupling is the temperature dependence of the mode's amplitude. This issue has already been discussed [24,47], but not in detail. In the analysis presented earlier [24,47], the peak amplitudes were discussed. Here, we will consider amplitudes as extracted by the Lorentzian line-shape analysis (i.e., the corresponding oscillator strengths), and compare them to the TDGL model simulations (see also Fig. 5 and the related discussion in Sec. IV).

Figure 7(a) shows the normalized (to their lowest-temperature data point) amplitudes of all observed modes in $K_{0.3}MoO_3$ up to ≈ 3 THz. When looking at the temperature dependence of amplitudes (oscillator strengths) of dominant modes (see also Fig. 5), we see that they are nearly constant up to ≈ 150 K. As elaborated in Sec. IV, such behavior can be expected for the case of linear coupling.

The weak mode at 1.35 THz has nearly the same temperature dependence and is therefore also likely to be linearly coupled to Δ . When including this mode in the TDGL model fit (as the fourth linearly coupled mode) we find that its coupling strength (m_4) is about an order of magnitude lower than those of the three dominant modes. The large difference in coupling strengths accounts for both the barely noticeable mode softening, as well as its low oscillator strength (see also Fig. 3 and the corresponding discussion in Sec. II). The polarization character of phonons at \mathbf{q}_{CDW} is neither fully transversal nor fully longitudinal. It is expected that phonons with different polarizations will have different coupling strengths to Δ , e.g., the lattice displacements in the CDW state found in x-ray diffraction [52] are mainly

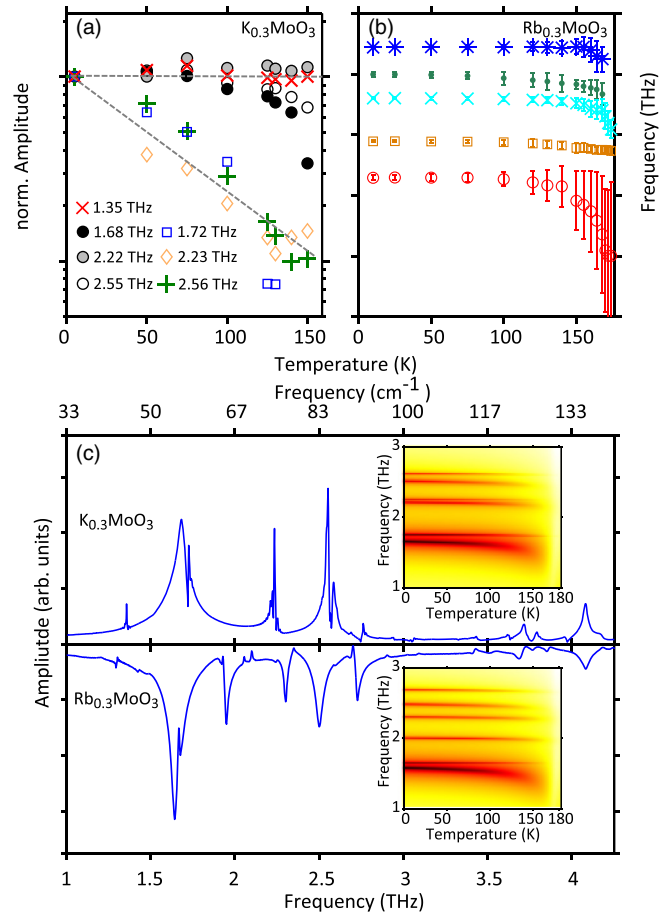


FIG. 7. (Color online) (a) The temperature dependence of the oscillator strengths of the modes (normalized to the corresponding values at the lowest temperature). (b) The temperature dependence of frequencies for the five most pronounced modes below 3 THz in $Rb_{0.3}MoO_3$. (c) The experimental spectra of $K_{0.3}MoO_3$ (top) and $Rb_{0.3}MoO_3$ (bottom) at ≈ 10 K. Insets present the corresponding simulated temperature dependencies, which are in very good agreement with experimental data (Ref. [24]).

perpendicular to the chain direction, while the Kohn anomaly is observed in a phonon branch of optical character with polarization along the chain direction [41]. From the low coupling strength of the 1.35-THz mode, we conclude that it originates from a phonon mode at $\pm \mathbf{q}_{CDW}$ whose eigenvector is nearly (but not completely) orthogonal to the periodic lattice displacements of the CDW state.

Several weak side modes in $K_{0.3}MoO_3$, which show only weak softening upon approaching T_c (see Fig. 1), display however a drop in their oscillator strengths by an order of magnitude [see Fig. 7(a)]. Such a behavior could be a signature of higher-order coupling nature of these modes. On the other hand, these three modes all lie in a close proximity to another (lower-energy) mode. And, as shown in Sec. II, in the case of two nearly degenerate modes with identical coupling strength to Δ , the higher-frequency one displays a much weaker softening (see Fig. 3).

To address this question experimentally, we performed the temperature-dependent study on $Rb_{0.3}MoO_3$, where the splitting between the high-frequency modes is substantially

larger [53]. The low-temperature (≈ 10 K) spectra for $\text{K}_{0.3}\text{MoO}_3$ and $\text{Rb}_{0.3}\text{MoO}_3$ are shown in Fig. 7(c). The low-frequency modes ($\nu < 2$ THz) resulting from coupling with acoustic phonons [33] at \mathbf{q}_{CDW} are in $\text{Rb}_{0.3}\text{MoO}_3$ just slightly red-shifted compared to $\text{K}_{0.3}\text{MoO}_3$ (as expected due to the higher atomic mass of Rb). The two nearly degenerate doublets of $\text{K}_{0.3}\text{MoO}_3$ at ≈ 2.2 and ≈ 2.55 THz, resulting from coupling of Δ with optical phonon branches, are however split up into four well-separated modes in $\text{Rb}_{0.3}\text{MoO}_3$. Unlike in $\text{K}_{0.3}\text{MoO}_3$, where in both doublets the higher-frequency modes show nearly no softening, all four modes soften in $\text{Rb}_{0.3}\text{MoO}_3$, as shown in Fig. 7(b). This suggests that all of the low-temperature non-Goldstone modes observed in *blue bronzes* result from *linear* coupling of normal modes (normal-state \mathbf{q}_{CDW} phonons) to Δ .

This assignment is further supported by model simulations for both compounds, which are shown in insets to Fig. 7(c). For the case of $\text{K}_{0.3}\text{MoO}_3$, we assumed to have three pairs of nearly degenerate phonon modes as observed in the experiment. For each doublet, we assumed that both modes have identical coupling strengths (m_i). The simulated temperature dependence closely reproduces the experimental data. In each doublet, the lower-frequency mode shows pronounced softening, while the higher-frequency mode does not. For simulating $\text{Rb}_{0.3}\text{MoO}_3$, we adjusted the mode frequencies to match the experimentally determined values, while keeping the coupling constants the same as for $\text{K}_{0.3}\text{MoO}_3$. As soon as the mode frequencies are split (only the four modes derived from optical phonon branches are split, while the modes at 1.6 THz remain nearly degenerate), they all show softening and linewidth broadening upon approaching T_c , as observed experimentally.

Furthermore, it follows from simulations that the temperature dependence of the oscillator strengths of modes also depend on the mode splitting. For the case of well-separated modes, as in $\text{Rb}_{0.3}\text{MoO}_3$, all high-frequency modes show similar temperature dependence (oscillator strengths nearly constant up to 150 K). For the case of nearly degenerate modes, as in $\text{K}_{0.3}\text{MoO}_3$, the higher-lying modes of each doublet show a pronounced decrease in the oscillator strength as observed in the experiment. Here, a quick note regarding the insets to Fig. 7(c) is in order. Due to the increasing linewidth of the lower-lying modes of the doublets, it may seem as if their oscillator strengths are decreasing with temperature. However, they remain nearly constant (the oscillator strength is determined by the product of peak amplitude and its width). In contrast, for the higher-lying modes in doublets, their linewidths remain nearly unchanged with increasing temperature, thus a decrease in peak amplitude indeed corresponds to a decreasing oscillator strength.

Finally, as shown in Fig. 7(c) (see also Refs. [24] and [47]), there are numerous additional modes above 3 THz which couple to Δ . Most of them show weak temperature dependence. This is expected since higher-frequency modes show generally weaker softening compared to the lower-frequency ones even for the case of comparable coupling strengths to Δ (see Sec. II). The exception is the mode at 4.07 THz, which shows strong softening [24,47] and thus seems to be very strongly coupled to Δ .

To summarize, we have shown that in $\text{K}_{0.3}\text{MoO}_3$ ($\text{Rb}_{0.3}\text{MoO}_3$) all the non-Goldstone modes (at least up to

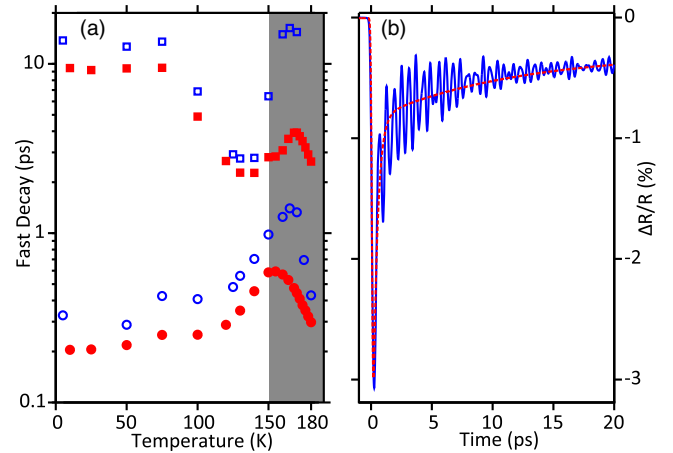


FIG. 8. (Color online) (a) The temperature dependence of the damping times extracted by fitting the overdamped part of the reflectivity transients in $\text{K}_{0.3}\text{MoO}_3$ (open symbols) and $\text{Rb}_{0.3}\text{MoO}_3$ (solid symbols) with a double exponential decay. (b) Reflectivity transient recorded on $\text{Rb}_{0.3}\text{MoO}_3$ at 4 K (blue solid line) and the corresponding overdamped response (red dashed line).

3 THz) result via linear coupling of normal modes to Δ . Apart from the weakly coupled 1.35-THz mode, all these modes exhibit comparable coupling strengths to Δ . We conclude that in an incommensurate quasi-1D CDW higher-order coupling seems to be negligible.

VI. OVERDAMPED MODES

The discussion so far has focused on the nature of low-temperature oscillatory modes. For completeness, we now briefly address the overdamped components. The solid line in Fig. 8(b) presents the raw data taken on $\text{Rb}_{0.3}\text{MoO}_3$ at 4 K while the dashed line presents a two-component exponential fit to it. Similarly to $\text{K}_{0.3}\text{MoO}_3$, we find a fast (200–300 fs) and a slow (≈ 10 ps) time scale. It should be noted that the presence of two decaying components, one of the 100 fs and the other one on the ps time scale, seems to be a general feature in CDW systems.

The temperature dependencies of the two time scales for both $\text{K}_{0.3}\text{MoO}_3$ (open symbols) and $\text{Rb}_{0.3}\text{MoO}_3$ (solid symbols) are shown in Fig. 8(a). Close to the phase transition the time scales of both components become comparable which results in great uncertainty [denoted by the shaded area in Fig. 8(a)].

The characteristic slowing down of the fast component (circles) with increasing temperature is attributed to an overdamped amplitude mode of Δ (see also Fig. 1). As elaborately discussed in the Appendix, the fast component may contain a considerable contribution from the oscillatory components as well as of the normal-state electronic response. Especially at low temperatures these two contributions may overshadow the overdamped amplitude mode, which is expected to become faster as our time resolution. At temperatures above ≈ 100 K, however, a reasonable agreement between the experimentally measured time scale and the damping time from simulations is obtained.

The slower, picosecond decay time [squares in Fig. 8(a)] shows the opposite temperature dependence, decreasing with increasing temperature. We note that this time scale and its temperature dependence are comparable to the damping time of the collective modes [24]. This observation suggests that the picosecond process could be linked to incoherently excited collective oscillations.

VII. CONCLUSION

In this paper, we presented a detailed analysis of time-resolved optical data on blue bronzes ($\text{K}_{0.3}\text{MoO}_3$ and $\text{Rb}_{0.3}\text{MoO}_3$), prototype quasi-one-dimensional charge-density wave (CDW) systems. Owing to advances in femtosecond time-resolved optical methods, coherently excited low-energy modes can be probed with high dynamic range and frequency resolution. Moreover, the inherent access to phases of these coherent modes enables deeper insight into their microscopic origin. We used the time-dependent Ginzburg-Landau (TDGL) model to analyze the temperature-dependent reflectivity transients. Apart from analysis of the mode's frequencies and damping times [24], we focused on their amplitudes and phases. We demonstrated that the Raman-active (non-Goldstone) modes observed in the low-temperature CDW phase are all a result of *linear* coupling between the nesting driven conduction electron density modulation and the normal-state phonons at the CDW wave vector. The true soft mode of the system was found to be an overdamped mode, which is mostly electronic in nature. By analyzing the temperature dependencies of oscillator strengths and phases of the individual modes, we were able to show that photoexcitation initially suppresses the electronic order-parameter component, while the response being probed by visible pulses is dominated by phonon-driven modulation of dielectric function (e.g., via modulation of the interband transitions caused by lattice vibrations). With this model, we can simulate the temperature-dependent reflectivity transients following photoexcitation with femtosecond pulses. The overall agreement between the simulations and experimental data is better than expected (see Fig. 10), considering the simplicity of the underlying assumptions.

This approach can be readily extended to more complex systems with spatially modulated ground states.

ACKNOWLEDGMENTS

We would like to thank K. Biljakovic, L. Degiorgi, T. Dekorsy, A. P. Levanyuk, J. E. Lorenzo, P. H. M. van Loosdrecht, T. Mertelj, D. Mihailovic, P. Monceau, V. Pomjakushin, J. P. Pouget, and D. Staresinic for valuable discussions. Financial support was given by the Carl Zeiss foundation, the Zukunftskolleg of the University of Konstanz, and the Alexander von Humboldt foundation.

APPENDIX: EXCITATION WITH A TIME-DEPENDENT (REALISTIC) DRIVING FORCE

In Sec. IV, it was shown that photoexcitation with a visible light pulse is most likely to initially perturb the EOP via

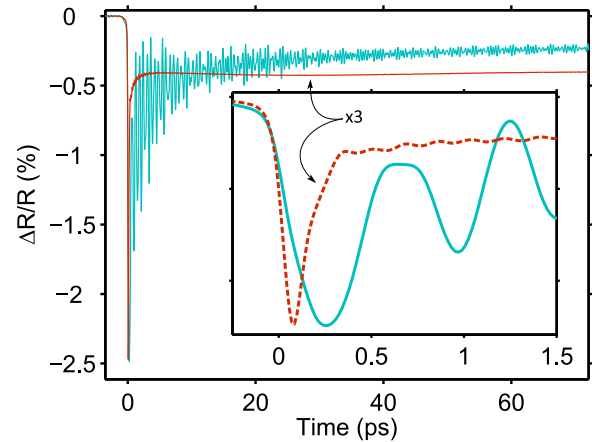


FIG. 9. (Color online) Transient reflectivity change at 1.55 eV after excitation of blue bronze with a 50-fs optical pulse. Solid cyan line presents the response in the CDW phase (10 K), while the dashed red line presents the data in the metallic phase (300 K). Inset: the same data zoomed in.

generation of excess quasiparticles. In the first approximation we considered a light pulse to be infinitely short, while the quasiparticle recovery time was infinite in comparison with damping times of the oscillatory modes (i.e., the driving force was a step function). Here, we consider a light pulse with a finite width generating excess quasiparticle density (EQD) with realistic recovery dynamics. A good first approximation for the EQD dynamics can be found in the time-resolved data in the metallic phase ($T > T_c$). In Fig. 9, the measured transient reflectivity change in the CDW (solid cyan line) and metallic (red dashed line) phases are shown. Comparison of rise times in both data sets shows that the initial response in the metallic phase is limited by the experimental time resolution (~ 70 fs), while the rise time in the CDW phase is about 200 fs.

In the metallic phase, the dynamics of the reflectivity transient is mainly linked to the EQD dynamics. The time evolution of the EQD can therefore be described by an instantaneous rise (limited by the pulse duration) and a subsequent recovery on a 100-fs time scale. Following this rapid thermalization of the electronic and lattice subsystems, the overall temperature of the excited volume is somewhat higher than the temperature before photoexcitation. The recovery dynamics is governed by the heat diffusion and proceeds on a time scale of tens of nanoseconds. This bolometric response $H(t)$, describing the temporal evolution of the temperature increase, can be considered to be a slow, adiabatic, process. Since by increasing temperature the equilibrium positions are also shifted, the equations of motion, Eq. (17), have to be extended to include the (adiabatic) temporal evolution of temperature. In the weak perturbation limit $H(t) \ll |T - T_c|$, resulting in

$$-\dot{\mathbf{x}} = \underline{\underline{M}} \begin{pmatrix} x(t) - \frac{\partial \Delta_0}{\partial T} H(t) \\ y(t) - \frac{\partial \xi_0}{\partial T} H(t) \\ z(t) \end{pmatrix} + \begin{pmatrix} F_\Delta(t) \\ 0 \\ F_\xi(t) \end{pmatrix}, \quad (A1)$$

where $\frac{\partial \Delta_0}{\partial T} = -\frac{\alpha}{2\beta\Delta_0}$ and $\frac{\partial \xi_0}{\partial T} = -\frac{\alpha m}{2\beta\Delta_0\Omega^2}$.

To retrieve the inhomogeneous solution of Eq. (A1), the equation was Fourier transformed:

$$\begin{aligned} i\omega \tilde{\mathbf{x}}(\omega) &= i\omega \begin{pmatrix} \tilde{x}(\omega) \\ \tilde{y}(\omega) \\ \tilde{z}(\omega) \end{pmatrix} \\ &= \underline{\underline{M}}[\tilde{\mathbf{x}}(\omega) - \tilde{\mathbf{h}}(\omega)] + \tilde{\mathbf{F}}(\omega). \end{aligned} \quad (\text{A2})$$

Here, $\tilde{\mathbf{h}}(\omega)$ describes the shift of the equilibrium values of Δ_0 (and ξ_0) due to the temperature variation, while the (coherent) driving forces are given by

$$\tilde{\mathbf{F}}(\omega) = \begin{pmatrix} \tilde{F}_\Delta(\omega) \\ 0 \\ \tilde{F}_\xi(\omega) \end{pmatrix}. \quad (\text{A3})$$

The solution of Eq. (A2) is given by

$$\begin{aligned} (i\omega + \underline{\underline{M}})\tilde{\mathbf{x}}(\omega) &= \tilde{\mathbf{F}}(\omega) - \underline{\underline{M}}\tilde{\mathbf{h}}(\omega) \\ \Rightarrow \tilde{\mathbf{x}}(\omega) &= (i\omega \underline{\underline{I}} + \underline{\underline{M}})^{-1}[\tilde{\mathbf{F}}(\omega) - \underline{\underline{M}}\tilde{\mathbf{H}}(\omega)] \end{aligned} \quad (\text{A4})$$

with I being the identity matrix.

Following the conclusions of Sec. IV, we assume that the coherent part of the driving force is primarily perturbing the EOP. Accordingly, we assume $F_\xi(t) = 0$ while $F_\Delta(t) = f_\Delta G(t)$. Here, $G(t)$ reflects the dynamics of EQD and is approximated by the dynamics observed in the high-temperature phase (Fig. 9), while the prefactor f_Δ describes the interaction strength. The decay component with the characteristic time scale of ≈ 4 ps which is found in the experiment [18] and briefly discussed in Sec. VI is not included in this simulation.

Figure 10 shows the reflectivity dynamics for different temperatures as observed in the experiment (upper panels) and the corresponding model simulations (lower panels). We should emphasize that the driving force was kept temperature independent in the simulation. The same goes for all the coupling constants, which were determined from the fit to the temperature dependence of frequencies and damping (see Fig. 1). Thus, the temperature dependence of transients comes solely from the temperature dependence of Δ via $\Delta = \sqrt{\frac{\alpha}{\beta}}(T_c - T)$. The time evolution of the coherent force $F_\Delta(t)$ and the bolometric contribution $H(t)$ are shown in the

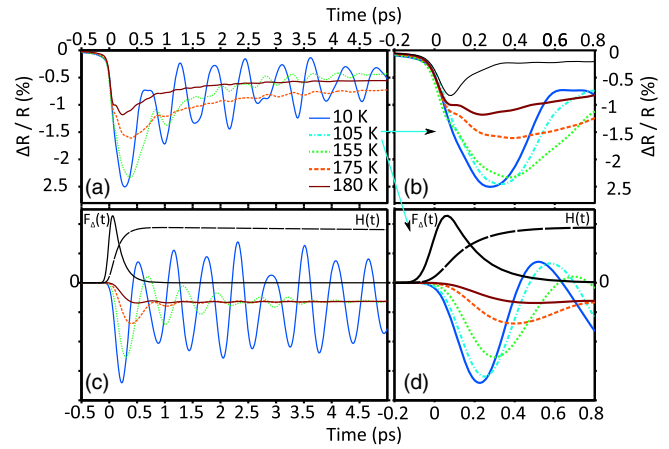


FIG. 10. (Color online) Photoinduced reflectivity transients recorded at several temperatures (upper panels) compared to model simulations (lower panels). The right panels present a zoom-in into the zero time delay region. The 105-K transient has been omitted in the left panels for clarity. In panel (b), an additional transient (thin solid line) presents the room-temperature data. The lower panels include the assumed coherent driving force (thin black line) and the bolometric response (black dashed line).

lower panels by the solid and dashed lines, respectively. The corresponding normal-state reflectivity transient is shown as a thin black line in Fig. 10(b).

Due to the restriction to only three modes in the simulation, some of the beating signatures appearing in the experiment are not reproduced (see, e.g., the low-temperature data in left panels). Second, the picosecond decay component is not included in the simulation. However, despite the above limitations, the overall agreement between the data and the simulation is astonishingly good. Focusing on the subpicosecond time dynamics (right panels), we observe that in the low-temperature CDW phase the rise time is longer and not limited by the experimental resolution. Moreover, both the experiment as well as the simulation reveal a clear increase in the rise time upon approaching T_c . Since photoinduced reflectivity changes seem to be dominated by the dynamics of the lattice component of the order parameter (see Sec. IV), the changes in the rise time can be associated to the temperature dependence of phase and damping of the most intense 1.68-THz mode, both resulting from coupling of the normal mode to EOP.

[1] M. Imada, A. Fujimori, and Y. Tokura, *Rev. Mod. Phys.* **70**, 1039 (1998).
 [2] A. I. Buzdin, *Rev. Mod. Phys.* **77**, 935 (2005).
 [3] M. Beck, M. Klammer, S. Lang, P. Leiderer, V. V. Kabanov, G. N. Gol'tsman, and J. Demsar, *Phys. Rev. Lett.* **107**, 177007 (2011).
 [4] N. Dean, J. C. Petersen, D. Fausti, R. I. Tobey, S. Kaiser, L. V. Gasparov, H. Berger, and A. Cavalleri, *Phys. Rev. Lett.* **106**, 016401 (2011).
 [5] C. Kübler, H. Ehrke, R. Huber, R. Lopez, A. Halabica, R. F. Haglund, Jr., and A. Leitenstorfer, *Phys. Rev. Lett.* **99**, 116401 (2007).

[6] A. Pashkin *et al.*, *Phys. Rev. Lett.* **105**, 067001 (2010).
 [7] H. Okamoto, T. Miyagoe, K. Kobayashi, H. Uemura, H. Nishioka, H. Matsuzaki, A. Sawa, and Y. Tokura, *Phys. Rev. B* **83**, 125102 (2011).
 [8] E. Möhr-Vorobeva, S. Johnson, P. Beaud, U. Staub, R. De Souza, C. Milne, G. Ingold, J. Demsar, H. Schaefer, and A. Titov, *Phys. Rev. Lett.* **107**, 036403 (2011).
 [9] M. Eichberger, H. Schaefer, M. Krumova, M. Beyer, J. Demsar, H. Berger, G. Moriena, G. Sciaini, and R. J. D. Miller, *Nature (London)* **468**, 799 (2010).

- [10] N. Erasmus, M. Eichberger, K. Haupt, I. Boshoff, G. Kassier, R. Birmurske, H. Berger, J. Demsar, and H. Schwoerer, *Phys. Rev. Lett.* **109**, 167402 (2012).
- [11] K. W. Kim, A. Pashkin, H. Schäfer, M. Beyer, M. Porer, T. Wolf, C. Bernhard, J. Demsar, R. Huber, and A. Leitenstorfer, *Nat. Mater.* **11**, 497 (2012).
- [12] D. Fausti, R. I. Tobey, N. Dean, S. Kaiser, A. Dienst, M. C. Hoffmann, S. Pyon, T. Takayama, H. Takagi, and A. Cavalleri, *Science* **331**, 189 (2011).
- [13] T. Kampfrath, A. Sell, G. Klatt, A. Pashkin, S. Mährlein, T. Dekorsy, M. Wolf, M. Fiebig, A. Leitenstorfer, and R. Huber, *Nat. Photonics* **5**, 31 (2011).
- [14] M. Beck, I. Rousseau, M. Klammer, P. Leiderer, M. Mittendorff, S. Winnerl, M. Helm, G. N. Gol'tsman, and J. Demsar, *Phys. Rev. Lett.* **110**, 267003 (2013).
- [15] R. Matsunaga, Y. I. Hamada, K. Makise, Y. Uzawa, H. Terai, Z. Wang, and R. Shimano, *Phys. Rev. Lett.* **111**, 057002 (2013).
- [16] G. Grüner, *Density Waves in Solids*, Frontiers in Physics, Vol. 89 (Westview Press, Boulder, CO, 1994).
- [17] P. Monceau, *Adv. Phys.* **61**, 325 (2012).
- [18] J. Demsar, K. Biljakovic, and D. Mihailovic, *Phys. Rev. Lett.* **83**, 800 (1999).
- [19] J. Demsar, L. Forró, H. Berger, and D. Mihailovic, *Phys. Rev. B* **66**, 041101 (2002).
- [20] K. Shimatake, Y. Toda, and S. Tanda, *Phys. Rev. B* **75**, 115120 (2007).
- [21] D. M. Sagar, A. A. Tsvetkov, D. Fausti, S. van Smaalen, and P. H. M. van Loosdrecht, *J. Phys.: Condens. Matter* **19**, 436208 (2007).
- [22] R. V. Yusupov, T. Mertelj, J.-H. Chu, I. R. Fisher, and D. Mihailovic, *Phys. Rev. Lett.* **101**, 246402 (2008).
- [23] A. Tomeljak, H. Schäfer, D. Städter, M. Beyer, K. Biljakovic, and J. Demsar, *Phys. Rev. Lett.* **102**, 066404 (2009).
- [24] H. Schäfer, V. V. Kabanov, M. Beyer, K. Biljakovic, and J. Demsar, *Phys. Rev. Lett.* **105**, 066402 (2010).
- [25] T. Mertelj, P. Kusar, V. V. Kabanov, P. Giraldo-Gallo, I. R. Fisher, and D. Mihailovic, *Phys. Rev. Lett.* **110**, 156401 (2013).
- [26] L. Perfetti, P. A. Loukakos, M. Lisowski, U. Bovensiepen, H. Berger, S. Biermann, P. S. Cornaglia, A. Georges, and M. Wolf, *Phys. Rev. Lett.* **97**, 067402 (2006); L. Perfetti, P. A. Loukakos, M. Lisowski, U. Bovensiepen, M. Wolf, H. Berger, S. Biermann, and A. Georges, *New J. Phys.* **10**, 053019 (2008).
- [27] F. Schmitt *et al.*, *Science* **321**, 1649 (2008).
- [28] F. Schmitt, P. S. Kirchmann, U. Bovensiepen, R. G. Moore, J.-H. Chu, D. H. Lu, L. Rettig, M. Wolf, I. R. Fisher, and Z.-X. Shen, *New J. Phys.* **13**, 063022 (2011).
- [29] T. Rohwer, S. Hellmann, M. Wiesenmayer, C. Sohr, A. Stange, B. Slomski, A. Carr, Y. Liu, L. M. Avila, M. Kallane, S. Mathias, L. Kipp, K. Rossnagel, and M. Bauer, *Nature (London)* **471**, 490 (2011).
- [30] J. C. Petersen *et al.*, *Phys. Rev. Lett.* **107**, 177402 (2011).
- [31] D. Mihailovic, D. Dvorsek, V. V. Kabanov, J. Demsar, L. Forró, and H. Berger, *Appl. Phys. Lett.* **80**, 871 (2002); T. Onozaki, Y. Toda, S. Tanda, and R. Morita, *Jpn. J. Appl. Phys.* **46**, 870 (2007).
- [32] H. Schaefer, M. Koerber, A. Tomeljak, K. Biljakovic, H. Berger, and J. Demsar, *Eur. Phys. J. Special Topics* **222**, 1005 (2013).
- [33] J. P. Pouget, B. Hennion, C. Escribe-Filippini, and M. Sato, *Phys. Rev. B* **43**, 8421 (1991).
- [34] V. A. Golovko and A. P. Levanyuk, *ZhETF* **81**, 2296 (1981) [*Sov. Phys.-JETP* **54**, 1217 (1981)].
- [35] G. Travaglini, I. Mörke, and P. Wachter, *Solid State Commun.* **45**, 289 (1983).
- [36] D. M. Sagar, D. Fausti, S. Yue, C. A. Kuntscher, S. van Smaalen, and P. H. M. van Loosdrecht, *New J. Phys.* **10**, 023043 (2008).
- [37] L. Degiorgi, B. Alavi, G. Mihály, and G. Grüner, *Phys. Rev. B* **44**, 7808 (1991).
- [38] R. Beyer, N. Barisic, and M. Dressel, *Phys. B (Amsterdam)* **407**, 1823 (2012).
- [39] M. J. Rice, *Phys. Rev. Lett.* **37**, 36 (1976).
- [40] O. V. Kovalev, *Irreducible Representations of the Space Groups* (Gordon and Breach, New York, 1965).
- [41] C. Escribe-Filippini, J. P. Pouget, R. Currat, B. Hennion, and J. Marcus, *Charge Density Waves in Solids*, Lecture Notes in Physics 217 (Springer, Berlin, 1985), pp. 71–75.
- [42] Y. A. Izyumov and V. N. Syromyatnikov, *Fazovyie Perekhody I Simmetriya Kristallov* (Nauka, Moscow, 1984) (in Russian).
- [43] J. Ollivier, J. Etrillard, B. Toudic, C. Ecolivet, P. Bourges, and A. P. Levanyuk, *Phys. Rev. Lett.* **81**, 3667 (1998).
- [44] In the strictly incommensurate case, where the phase transition is associated with a non-Lifshitz wave vector, the higher-order invariants which depend on the phase of the order parameter are absent. Thus, the thermodynamic potential does not depend on the phase of the order parameter (Refs. [42] and [43]).
- [45] D. G. Sannikov, *Phys. Solid State* **50**, 746 (2008).
- [46] G. Travaglini and P. Wachter, *Phys. Rev. B* **30**, 1971 (1984).
- [47] See Supplementary Material to Ref. [24] at <http://link.aps.org/supplemental/10.1103/PhysRevLett.105.066402>.
- [48] H. J. Zeiger, J. Vidal, T. K. Cheng, E. P. Ippen, G. Dresselhaus, and M. S. Dresselhaus, *Phys. Rev. B* **45**, 768 (1992).
- [49] R. Merlin, *Solid State Commun.* **102**, 207 (1997).
- [50] T. E. Stevens, J. Kuhl, and R. Merlin, *Phys. Rev. B* **65**, 144304 (2002).
- [51] K. Ishioka, M. Hase, M. Kitajima, L. Wirtz, A. Rubio, and H. Petek, *Phys. Rev. B* **77**, 121402 (2008).
- [52] M. Sato, H. Fujishita, S. Sato, and S. Hoshino, *J. Phys. C: Solid State Phys.* **18**, 2603 (1985).
- [53] A. Tomeljak, B. Kavcic, H. Schäfer, V. V. Kabanov, D. Mihailovic, D. Staresinic, K. Biljakovic, and J. Demsar, *Phys. B (Amsterdam)* **404**, 548 (2009).